Forward-Looking Ultrasound Imaging Transducer : I. Analysis and Design

전향 초음파 영상 트랜스듀서 : I. 해석 및 설계

Chankil Lee*
이 찬 길*

ABSTRACT

The transducer section of the forward-looking ultrasound imaging catheter (FLUIC) consists of a circular piezoelectric element as a vibrator and a conical acoustic mirror as a perfect reflector. A small diameter piezoelectric transducer element is mounted on the side of a catheter's rotating shaft. The unique design of FLUIC provides the capability to form a two-dimensional image of a cross-section of a vessel in front of the catheter, which is lacking in the present generation of intravascular ultrasound (IVUS) transducers, as well as a conventional side-view image. The mirror configuration for the transducer section of the FLUIC is designed using an approximated ray tracing techniques. The diffraction transfer function approach [1] developed for the field prediction from primary sources is generalized and extended to predict the secondary diffraction characterstics from an acoustic mirror. The extended model is verified by simulation and experiment through a simple plane reflector and employed to analyzed the field characteristics of a FLUIC.

요 약

전향 초음파 영상 캐서터의 트랜스듀서 (FLUIC) 부분은 진동자인 원형 전기음향 소자와 원뿔꼴 반사체인 음향 반사체로 구성된다. 소형의 전기음향 소자는 캐서터의 회전자 축 측변에 탑재된다. 전향 초음파 영상 캐서터의 특징은 기존의 IVUS 트랜스듀서가 제공할 수 없는 캐서터 전단에서 혈관의 단층 2-D 영상과 종래의 측면 영상을 동시에 제공하는 것이다. FLUIC의 트랜스듀서에 사용된 음향 반사체를 설계하기 위해 근사화된 레이 추적 기법을 이용하였다. 음향 반사체로 부터 2차 회절 특성을 예측하기 위해 회절전달함수방식에[1] 의한 1차 음원으로 부터의 장 예측모델을 확장하여 일반화 하였다. 확장된 모델은 단순한 평판 반사체에 적용하여 시뮬레이션과 실험에 의해 검증되었으며 FLUIC의 장 특성을 해석하는데 사용되었다.

I. Introduction

Current engineering efforts in intravascular ultrasound (IVUS) imaging are being directed principally at the refinement of image quality, improvement in catheter performance characteristics, and miniaturization of the catheters for effective use in the intravascular applications. Presently it is unclear which type of system, mechanical or multi-element as shown in Fig. 1, will be better accommodate miniaturization to a range of 3F~4F (1~1.3 mm diameter), which is required for imaging the distal coronary arteries. Currently, both mechanical and multi-element prototype catheters are in the 5F~6F (1.67~2.0 mm) range. Considering the current development, it is probable that image quality and resolution from the mechanical systems will be superior to the muti-element array approach. However, the mechanical catheter is slightly more rigid than the multi-element catheter, making it more difficult to thread through the vasculature.

However, the major shortcoming of the present generation of ultrasonic intravascular imaging

*한양대학교, 전자공학과
Department of Electronics Engineering, Hanyang University
접수일자 : 1995년 6월 1일

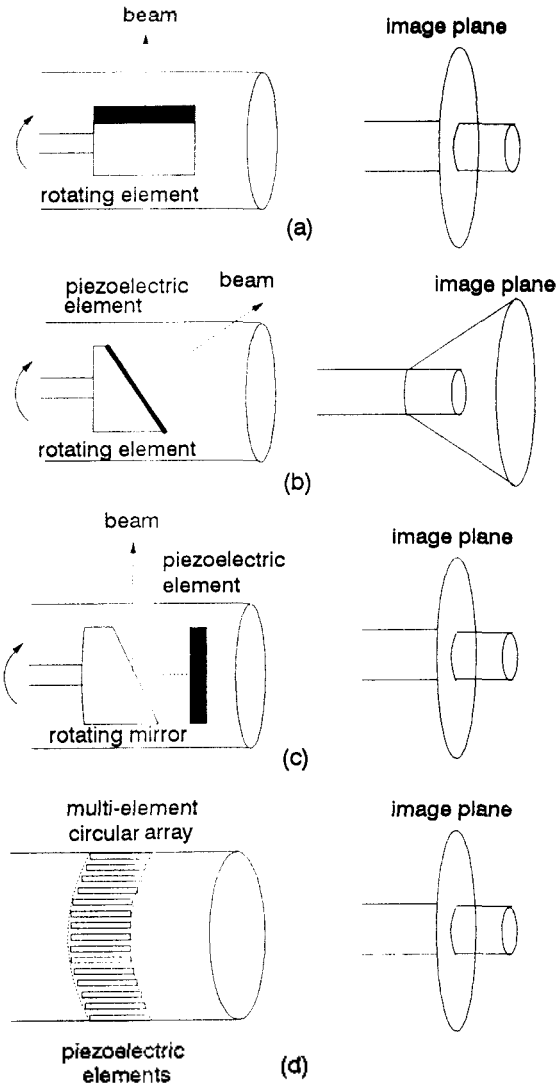

Fig. 1 Mechanically-rotated single-element oriented either at : (a) 90o with respect to the long axis of the catheter or ; (b) a slightly forward-looking angle. (c) mechanically-rotated mirror with respect to the long axis of the catheter ; (d) a multi-element circular array transducer.

catheters is their inability to look ahead, making it necessary to cross the lesion in order to image it. This prohibits the visualization of lesions which are large enough to block the passage of the imaging catheter. An imaging catheter which could look ahead and obtain a cross-sectional image in front of its tip would eliminate this problem. Furthermore, being able to look ahead will decrease the chance of vessel wall damage by the imaging catheter as it is guided through the vasculature. The look-ahead capability would also make it possible to steer the catheter away from treacherous bends or intimal dissections. Naturally, it is widely acknowledged that in order for this technology to achieve its full potential, a forward-looking imaging capability must be developed [2-4].

The objective of this work is to develop a new type of transducer for IVUS imaging applications. The unique design of this transducer, hereafter referred to as a forward-looking ultrasonic imaging catheter (FLUIC), provides the capability to form a two-dimensional image of a cross-section of a vessel *in front of* the catheter. This is a very important feature which is lacking in the present generation of IVUS transducers. The transducer section of the FLUIC consists of a circular piezoelectric element as a vibrator and a conical acoustic mirror as a perfect reflector. This configuration provides a line focused beam. The embodiment of this device is illustrated in Fig. 2.

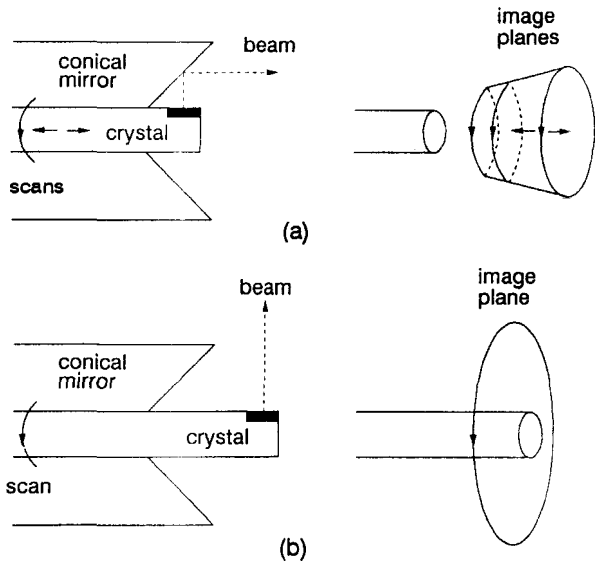

Fig. 2 Cut-away view of the FLUIC in : (a) forward-looking mode ; (b) side-view mode.

A small diameter piezoelectric transducer element is mounted on the side of a rotating shaft in a manner similar to that of several existing intravascular imaging catheters [3, 5]. However, in this case the ultrasonic pulse transmitted from the element reflects off of the conical mirror and propagates in the forward direction. The rotating shaft steers the transmitted pulse along an annulus whose diameter is controlled by vertical position of the shaft. The angle of the mirror is slightly less than 45° so that the reflected pulse travels at an angle toward the longitudinal axis of the catheter. This angulation enables

the imaging of the entire field in front of the catheter tip. The exact angle chosen will depend upon the minimum distance in front of the catheter one wishes to image. In the receive mode, the echo signals from the lesion are reflected off the mirror back to the transducer element. Several types of image formats can be produced by controlling the motion (rotational and translational) of the shaft and the timing of the pulser/receiver. For example, both cross-sectional and longitudinal 2-D slices of the vessel can be imaged as shown in Fig. 2. The FLUIC could also be capable of acquiring 3-D image data in non-coronary vasculature. However, 3-D imaging in the coronary arteries would require a long data acquisition time, relative to the motion of the walls of the heart, that would subject it to severe motion artifacts.

In this paper, a new mirror configuration for IVUS imaging applications was designed and its field characteristics were analyzed. First, a large-scale version of the FLUIC was designed. Second, the diffraction transfer function approach developed in [1, 6] was extended to the analysis of the acoustic reflection and diffraction problems. The developed model was employed to analyze the field characteristics of a FLUIC.

II. Design of the Large-Scale FLUIC

In general, the ultrasonic beam from a single transducer can be controlled by three methods, namely, the use of a shaped transducer, an acoustic lens, and a mirror. The conventional focused transducers use either spherically shaped piezoelectric transducer elements [7-9] or acoustic lenses to focus the beam. Alternatively, acoustic mirrors have also been used to focus or reflect the beam in an acoustic microscopy and imaging applications [7, 10, 11]. For this investigation, a new mirror geometry was devised to enable both forward and cross-sectional scanning capabilities in an IVUS transducer [12]. The reflection and refraction at the mirror surface is considered to avoid acoustic reverberations. The acoustic field characteristics and the shape of the piezoelectric element are used to determine the constraints on the forward-looking mirror geometry. The approximated ray tracing techniques, similar to those employed in optics, are developed to analyze the reflected beam patterns of the mirror.

1. Mirror Reflection and Refraction

In the design of an acoustic mirror it is important to avoid reverberations which give rise to standing waves between the transducer element and mirror. Some of the incident energy transmitted into the mirror may be reflected off its rear surface and pass back to the transducer after two or more transits through the mirror. This causes multiple pulses to be transmitted and multiple echoes are received. The appropriate mirror can be chosen from material with a high acoustic impedance relative to water to act as good reflector. Table 1 shows the various acoustic impedance of the solids. Stainless steel was chosen for this application because of its high acoustic impedance and ease of machining. The mirror surface is also to be as smooth, compared to a wavelength, as possible to avoid acoustic reverberation during wave incidence. Accordingly, the reflected wave can be well defined in such a specular reflection.

The reflection and refraction of an incident plane wave from its interaction with a plane reflector is illustrated in Fig. 3 (a). The acoustic mirror is assumed to be constructed of many plane reflectors. The incident wave at each acoustic window is treated locally as a plane wave for the acoustical field calculation presented in the next chapter. In

Table 1. Bulk material constants for selected solids.

Material	V_l (km/s)	V_s (km/s x 10^3)	ρ_o (kg/m^3 x 10^6)	Z_l (kg/m^2-s x 10^6)
Aluminum	6.42	3.04	2.70	17.33
Glass(Pyrex)	5.64	3.28	2.24	31.1
Gold	3.24	1.20	19.7	63.8
Silver	3.6	1.6	10.6	38.0
Steel, mild	5.9	3.2	7.9	46
Steel, stainless	5.79	3.1	7.89	45.7
Tungsten	5.2	2.9	19.4	101

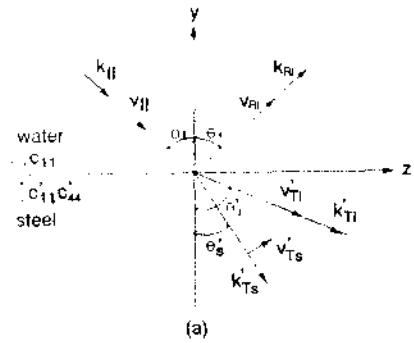

(a)

(b)

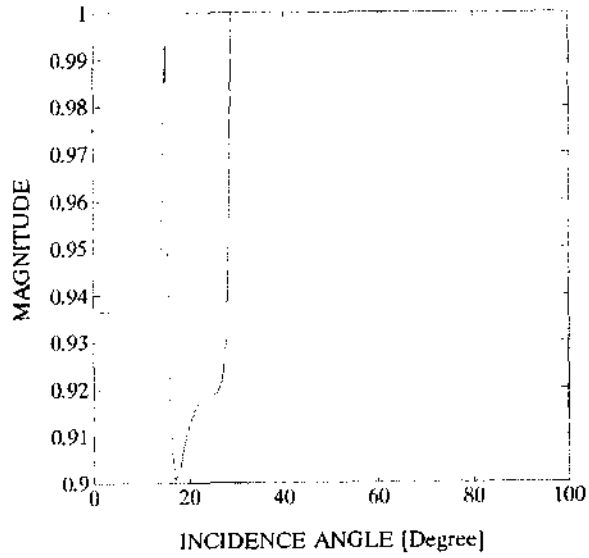

Fig. 3 Reflection and refraction of longitudinal wave at plane boundary. (a) Reflection and refraction between isotropic media. (b) Reflection coefficients for a longitudinal wave incident on a boundary between water and stainless steel.

this case, the particle velocity associated with the transmitted, reflected, and incident waves into each acoustic window are

$$\mathbf{v}_{II}=\frac{\mathbf{k}_{II}}{k_I}\,\boldsymbol{A}_I\exp^{-i\mathbf{k}_{II}\cdot\mathbf{r}},\quad \mathbf{v}_{RI}=\frac{\mathbf{k}_{RI}}{k_I}\,\boldsymbol{A}_I\exp^{-i\mathbf{k}_{RI}\cdot\mathbf{r}}$$

$$\mathbf{v}'_{II}=\frac{\mathbf{k}'_{TI}}{k'_I}\,\boldsymbol{B}'_I\exp^{-i\mathbf{k}'_{TI}\cdot\mathbf{r}},$$

$$\mathbf{v}'_{Ts}=\frac{-\mathbf{k}\times\mathbf{k}'_{Ts}}{k'_s}\,\boldsymbol{B}'_s\exp^{-i\mathbf{k}'_{Ts}\cdot\mathbf{r}} \tag{1}$$

where the subscripts l and s denote longitudinal and shear waves, respectively.

The particle velocity and stress must be continuous at all points on the boundary,

$$\mathbf{v}=\mathbf{v}',\quad \mathbf{T}\cdot\mathbf{n}=\mathbf{T}'\cdot\mathbf{n}'. \tag{2}$$

From Eq.(1) and Fig. 3 (a), the continuity of vy and vz at y=0 gives the boundary value equations. Only two stress components, T_{yy} and T_{yz}, are relevant to the boundary condition. The boundary conditions can then be simplified

$$c_{11}=c_{12}+2c_{44},\ c_{21}=\lambda,\ c_{44}=\mu \tag{3}$$

and Snell's law,

$$k_z=k_l\sin\theta_l=k'_l\sin\theta'_l=k_s\sin\theta_s=k'_s\sin\theta'_s. \tag{4}$$

These substitutions lead to the set of reflection and refraction equations [13]

$$\begin{aligned}
-A_l\cos\theta_l &= -B_l\cos\theta_l-B'_l\cos\theta'_l+B_s\sin\theta_s+B'_s\sin\theta'_s\\
-A_l\sin\theta_l &= -B_l\sin\theta_l+B'_l\sin\theta'_l-B_s\cos\theta_s+B'_s\cos\theta'_s\\
A_lk_l(\lambda+2\mu\cos^2\theta_l) &= -B_lk_l(\lambda+2\mu\cos^2\theta_l)\\
&\quad +B'_lk'_l(\lambda'+2\mu'\cos^2\theta'_l)\\
&\quad +B_s\mu k_s\sin(2\theta_s)\\
&\quad -B'_sk'_s\mu'\sin(2\theta'_s)\\
-A_lk_l\mu\sin(2\theta_l) &= -B_lk_l\mu\sin(2\theta_l)-B'_lk'_l\mu'\sin(2\theta'_l)\\
&\quad +B_s\mu k_s\cos(2\theta_s)\\
&\quad -B'_sk'_s\mu'\cos(2\theta'_s)
\end{aligned} \tag{5}$$

The reflection and transmission coefficient are

$$\Gamma_{II}=\frac{B_I}{A_I}=\frac{\Delta_{II}}{\Delta},\ \Gamma'_{II}=\frac{B'_I}{A_I}=\frac{\Delta'_{II}}{\Delta},\ \Gamma'_{sI}=\frac{B'_s}{A_I}=\frac{\Delta'_{sI}}{\Delta} \tag{6}$$

Here Δ is the determinant of the coefficient on the right side of Eq. (5). Δ_{II} is the determinant obtained by replacing the coefficient of B_l with those of A_l, etc.

Critical angles may be calculated and quantitative information on the reflection amplitudes can be deduced from these relations. Consider the incident medium as water and transmitting medium as stainless steel. For water, $v_l=1497m/s$ and $\rho_{mo}=10^3\ kg/m^3$. For stainless steel, $v_l=5790\ m/s$, $v_s=3100m/s$, and $\rho_{mo}=7.89\times10^3\ kg/m^3$. For this boundary, the critical angle for a transmitted longitudinal wave is $\theta_{cl}=\sin^{-1}(v_{II}/v_{Tl})=150°$ and the critical angle for a transmitted shear wave is $\theta_{cs}=\sin^{-1}(v_{II}/v_{Tl})=29°$ as shown in Fig. 3 (b). Therefore, for the case of $\theta_i>\theta_{cs}$, all the incident energy is reflected off into the incident medium in the process known as total internal reflection.

2. Conical Mirror

Figure 4 illustrates the geometry of the FLUIC. A small piezoelectric disk of radius r_a, is mounted on the end of a rigid rod, of radius r_n, at a height of r_t. The rod is inserted through a snug hole in a cylindrical stainless steel bar to provide a stable bearing surface necessary for an accurate rotational and translational scanning. The end of the bar is machined to form a conical reflector with outer diameter of rm, inner diameter of r_n, and angle of r_m, inner diameter of r_m, and angle of ϕ.

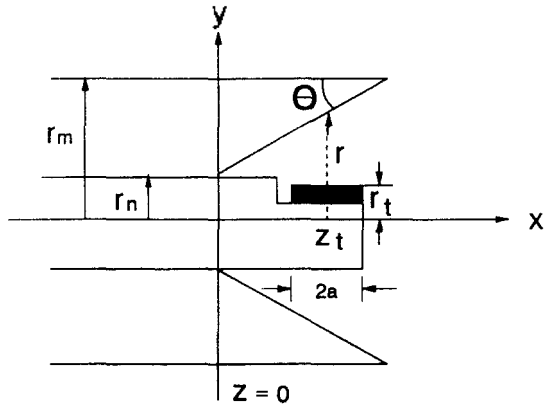

(a) side-view

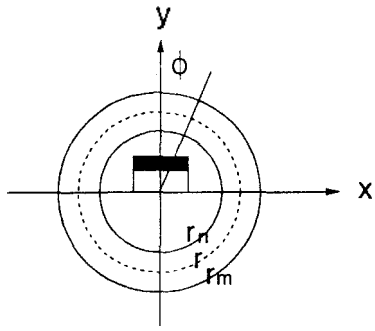

z = zt

(b) front-view

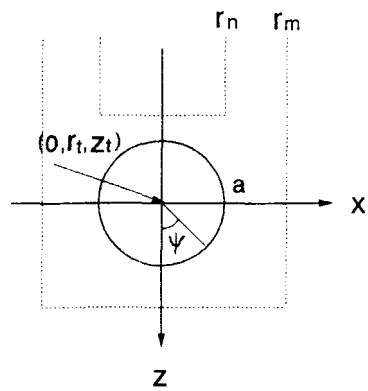

(c) top-view

Fig. 4 Geometry used for a conical mirror. (a) Side-view, (b) Front-view, (c) Top-view.

The surface function of the conical mirror is described by $x=r\sin\phi$, $y=r\cos\phi$, where $0\leq\phi\leq 2\pi$. The curvatures of a conical mirror r depend on the angle θ at the z,

$$r=z\tan\theta+r_n \cdots \quad (7)$$

The surface of the transducer element centered at (r_t, z_t) is given by

$$x=r_a\sin\psi,\ y=r_t,\ z=z_t+r_a\cos\psi, \quad (8)$$

where $0\leq\psi<2\pi$.

The geometrical design of the mirror must allow for both steering and focusing. The transducer element should not touch the mirror as it is steered. This condition gives the relationship between θ and r_t for a specified r_a, z_t, and r_n

$$z_t\sin\theta+r_n\cos\theta=\sqrt{r_t^2+r_a^2}. \quad (9)$$

The mirror should be within the near-far field region of a transducer element so as to enable the beam to be collimated. This limits the maximum diameter of the mirror to

$$r_m<r_a^2/\lambda+r_t. \quad (10)$$

This condition guarantees that mirror is in the region of beam collimation and the incident beam is guided effectively with a mirror. Rays reflected back toward the transducer plane from the surface of the mirror may be calculated computationally for reverberation considerations. This computation including the reflectivity at each mirror point can provide the approximated sensitivity of the FLUIC defined by the ratio of reflected energy into the forward direction to the radiated energy from a transducer. Using the loose condition that the reflected wave from the innermost rays not propagate back to the transducer element, the mirror angle θ must satisfy the condition,

$$\left[(z_t-r_a)\tan\theta+(r_n-r_t)\right]\tan 2\theta>2a. \quad (11)$$

Finally, the angle of the mirror must be slightly less than 45o so that the reflected pulse travels at a angle towards the longitudinal axis of the catheter.

Using the above conditions, the design parameters selected for a large-scale version of the FLUIC, operating at 2 MHz, were : $r_a = 6\lambda = 4.5$mm, $\theta = 45°$, $r_t = 7.3\lambda = 5.5$mm, $r_n = 10\lambda = 7.5$mm, and $r_m = 30\lambda = 22.5$mm.

3. Ray Tracing Method

A ray tracing method, similar to those employed in optics, was adapted to aid in the analysis of the reflected beam patterns from the mirror. A computer program to trace the rays was developed to study how the shape of the mirror affects the acoustic field.

In the program, a point is chosen to represent each of the incremental sources in the transducer element. Rays leaving these points at different angles are traced through the mirror using the reflection law at each interface to produce the reflected rays, assuming total internal reflection is assumed at each mirror point. The conical mirror of the FLUIC can be considered as consisting of an ensemble of spherical curvatures. A zero-order paraxial approximation of the mirror formula is given by

$$\frac{1}{s_o} + \frac{1}{s_i} = -\frac{2}{r} \tag{12}$$

where r is the curvature of the concave ($r<0$) spherical mirror, s_o and s_i are the source and image distance measured from the vertex. This formula can not be used for this geometry since the curvatures of the mirror are not much larger than the diameter of the transducer element. Thus, the sources which are not in a paraxial region produce spherical aberations in both the lateral and axial dimensions, as shown in Fig. 5.

In addition, the FLUIC geometry does not have symmetry at the optical axis due to the varying curvature of the conical mirror. For the above reasons, the ray tracing method is of little value for the quantitative analysis of the FLUIC's mirror system. However, this method is useful for qualitative estimations of the ray pattern if only center rays from the circumference of the transducer are traced. Figure 6 (a) shows the results of the ray tracing for a conical mirror in the $x=0$ plane. The direction of the the reflected rays will be determined by the mirror

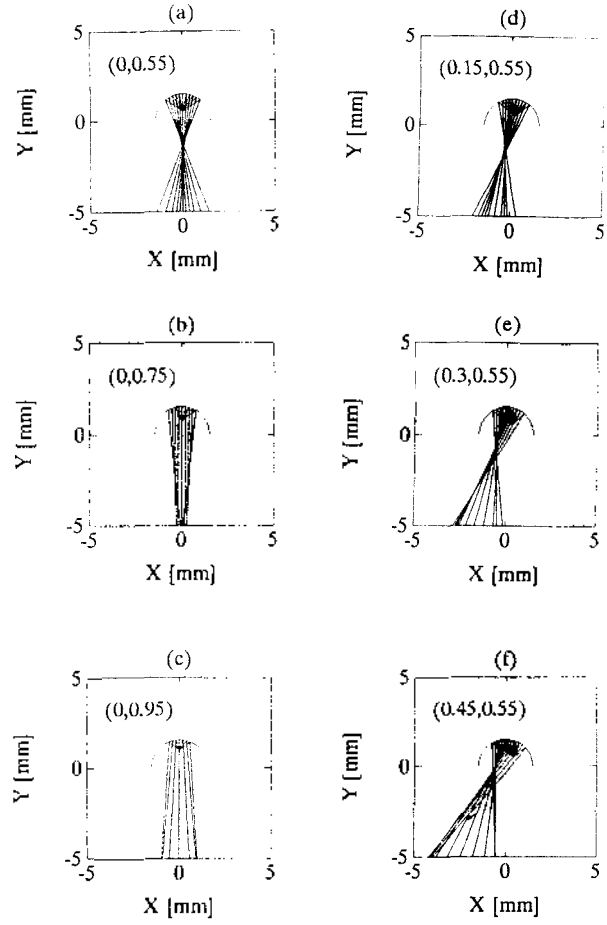

Fig. 5 Reflected rays (-60°~60°) from a concave spherical mirror with curvature of 1. 5mm. (a)-(c) Source at on-axis ($x=0$ and $y=0.55$, 0.75, 0.95mm). (d)-(f) Source at off-axis ($x=0.15$, 0.3, 0.45mm and $y=0.55$mm).

angle θ.

To trace the rays in the xy plane, suppose the transducer consists of many line sources. The curvature of the conical mirror and the length of the line sources in a circular piston will vary according to Eq. (7) and Eq. (8), respectively. Figure 6(b) shows the reflected rays from many line sources in the transducer. From the lens formula, the incident beam on the each concave spherical mirror with the curvature r, in the paraxial range, will be focused at $F = r/2$. From this approximate ray tracing, the focal region will be formed around 20λ. At greater depth, the focal region the beam will be defocused, in a manner similar to the beam from a spherical radiator. From this result, the overall pattern will have a larger beamwidth on the bottom half than the top half due to the greater defocusing of the beam from the smaller curvature of the mirror.

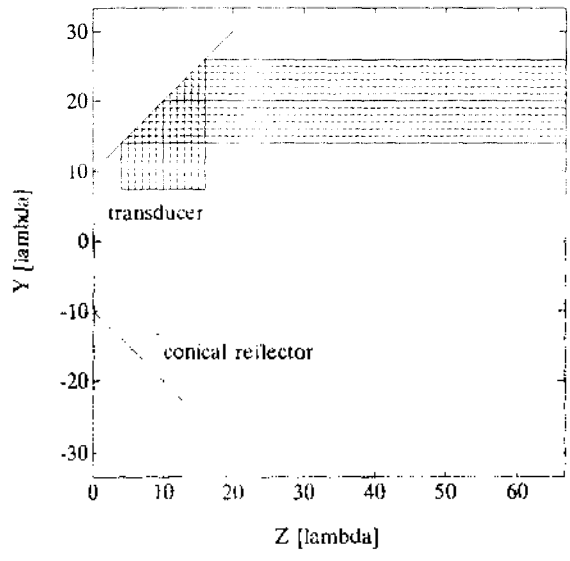

(a)

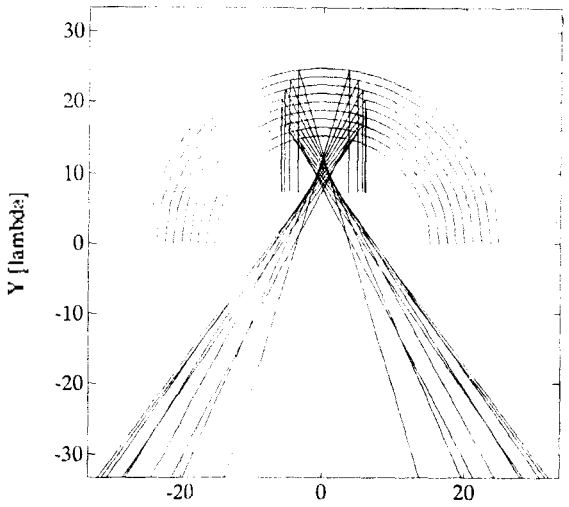

(b)

Fig. 6 The approximate ray tracing from a transducer centered at ($r_t = 5.5$mm, $z_t = 7.5$mm) in the : (a) $x = 0$ plane ; and (b) xy plane.

Ⅲ. Acoustical Field Calculations

In the design of an acoustic mirror (acoustic reflection problem) or aperture/lens based (acoustic diffraction problem) systems, various approaches have been taken to characterize the acoustic field. Simple ray tracing methods from geometric optics were used in the calculation of the focal point [11, 14]. A combination of wavefront and wave optics were used for estimating the performance in acoustic microscopy [15]. The method of stationary phase was adopted to avoid difficulties in mathematical analysis and the expressions for the light intensity distributions in the axial and off-axis images of a point source on the axis of reflecting cone have been derived [16]. Huygens' principle, which regards the lens surface as points sources which serve as a secondary wavelet sources, has been used to determine the field intensity pattern from an ultrasonic transducer with a lens [17]. This method provides better accuracy at the expense of computational efficiency.

In this section, the diffraction transfer function approach discussed in [1] is generalized and extended to predict the imaging characteristics of mirror/lens based imaging systems and investigate the effects of the mirror/lens on the field characteristics. Since the inputs to this extended model include the shape of the excitation signal, the geometry of the transducer (primary source) and mirrors/lens (secondary source), and the characteristics of the transmitting medium, the results obtained can be used to accurately predict the beam characteristics. The developed model was verified by simulation and experiment through a simple plane reflector and employed to analyze the field characteristics of a FLUIC.

1. Extension of the Diffraction Transfer Function Approach

To predict the field characteristics of the FLUIC, an extended version of the diffraction transfer function approach was employed. The general Helmholtz-Kirchhoff integral over a surface, as illustrated in Fig. 7, formed approach was employed. The general Helmholtz-Kirchhoffintegral over a surface, as illustrated in Fig. 7, formed by a transducer aperture T and the secondary surface $M+N$, is expressed using a velocity potential function ϕ_ω. Two common simplifying assumptions are used. First, on the non-illuminated side of the secondary surface N, ϕ_ω and $\nabla\phi_\omega$ are assumed to be negligible known as Kirchhoff's boundary conditions [18]. Second, the contribution from the enclosing surface, B, is assumed to be negligible, known as the Sommerfeld radiation condition. Using these assumptions, the potential at a field point in time-independent form is given by

$$\phi_\omega(\mathbf{r}) = \left[\int_T + \int_M\right]\{\phi_\omega(\mathbf{r}_0)\nabla G_\omega(\mathbf{r}\mid\mathbf{r}_0) - G_\omega(\mathbf{r}\mid\mathbf{r}_0)\nabla\phi_\omega(\mathbf{r}_0)\}\cdot\mathbf{n}dS_0 \qquad (13)$$

where $\mathbf{n}$ is the normal vector pointing outward from the surface.

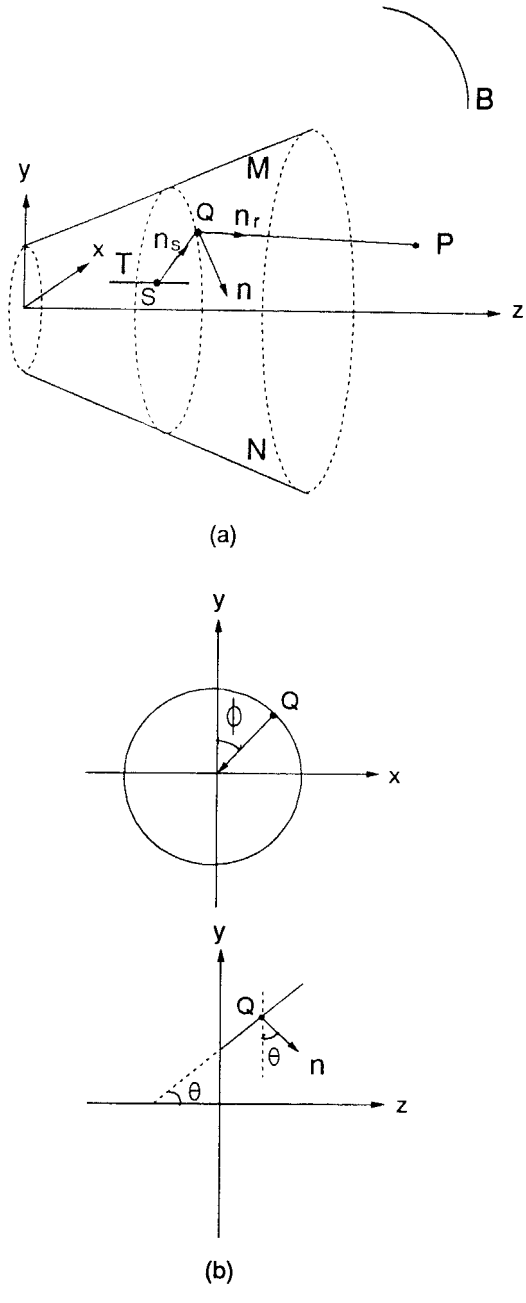

Fig. 7 The ray geometry corresponding to the Helmholtz-Kirchhoff's formular. (a) Wave vector. (b) Normal vector.

If the medium is bounded by some surface on which boundary conditions are imposed, the free-space Green's function $g_\omega(\mathbf{r}|\mathbf{r}_o)$, cannot be used. Thus, a general Green's function $G_\omega(\mathbf{r}|\mathbf{r}_o)$, which satisfies the inhomogeneous Helmholtz equation should be used in order to satisfy the appropriate boundary conditions. Moreover, $G_\omega(\mathbf{r}|\mathbf{r}_o)$ represents that the total field at r is the summation of the fields from all the elementary sources in the transducer plus the waves reflected by the boundary surface. However, when the field of interest is far off-axis, the effect of beam contributions from a direct propagation is negligible if the beam is well collimated. Thus, only the scattered field need be considered for the FLUIC geometry.

$$\phi_s(\mathbf{r}) = \int_M \{\phi_\omega(\mathbf{r}_o)\nabla G_\omega(\mathbf{r}|\mathbf{r}_o) - G_\omega(\mathbf{r}|\mathbf{r}_o)\nabla\phi_\omega(\mathbf{r}_o)\}\cdot\mathbf{n}dS_o \tag{14}$$

The Helmholtz-Kirchhoff integral, based on Huygens' principle, can be transformed into an approximated diffraction integral representing classical cases of planar acoustic boundary conditions as in [1]. Therefore, to calculate the scattered field from a transducer with acoustical mirrors, the wavefront at the mirror surface is treated as a secondary source and the total field at P is constructed from the mutual interference of the secondary wavelets.

In order to discuss the conical mirror system, a rectangular-coordinate system (x, y, z) is introduced with its origin O at the center of the cone which has the same radius of shaft, and z-axis as shown in Fig. 7 (a). The distance from the mirror surface $Q(x, y, z)$ to the point source $S(x_t, y_t, z_t)$ in the transducer and to the point $P(x_p, y_p, z_p)$ in the image plane are s and r, respectively. For a continuous wave which propagates from a point source S through an acoustic window at the center of Q, the normal vector at Q

$$\mathbf{n} = -\cos\theta(\sin\phi\mathbf{x} + \sin\phi\mathbf{y}) + \sin\theta\mathbf{z} \tag{15}$$

where θ and ϕ is described in Fig. 7 (b). For the plane reflector case where $\phi = 0$, the normal vector is given by $\mathbf{n} = -\cos\theta\mathbf{y} + \sin\theta\mathbf{z}$.

A. Free-Space Secondary Source

The values of ϕ_ω and $\nabla\phi_\omega$ on T and M which are necessary in evaluating the Helmholtz-Kirchhoff integral are never known exactly. However, it is reasonable to assume that everywhere on M, except in the immediate neighborhood of the rim of the opening, ϕ and $\Delta\phi$ will not appreciably differ from the values obtained in the absence of the aperture. Thus, additional contribution arising from the vicinity of the aperture's edge, known as the boundary diffrac-

tion wave, is ignored in this analysis. The Kirchhoff's diffraction integral using a free-space Green's function can then be reduced to

$$\phi_s(\mathbf{r}) = -\frac{jk}{4\pi^2}\int_M \frac{\exp^{-jkr}}{r}\left[\int_T \frac{\exp^{-jks}}{s} dT\right]\mathbf{n}\cdot\mathbf{n}_r dM - \int_M \frac{\exp^{-jkr}}{r}\left[\int_T \frac{\exp^{-jks}}{s}\mathbf{u}\cdot\mathbf{u}_s dT\right]dM \quad (16)$$

The components in the brackets, secondary wavelets, are to be computed for the calculation the scattered field.

B. Soft Secondary Source

For this case, which is similar to the radiation case, if a free space Green's function and out-of-phase mirror image source are chosen, the Kirchhoff's diffraction integral reduces to

$$\phi_s(\mathbf{r}) = -\frac{jk}{4\pi^2}\int_M \frac{\exp^{-jkr}}{r}\left[\int_T \frac{\exp^{-jks}}{s} dT\right]\mathbf{n}\cdot\mathbf{n}_r dM \quad (17)$$

C. Rigid Secondary Source

The source distribution of velocity potential, ϕ, on the mirror surface can be calculated using the Rayleigh integral formula. The velocity at the mirror surface, $\mathbf{u}_t$, can then be determined by the gradient of the velocity potential distribution

$$\mathbf{u}_t(x, y, z) = \nabla\phi_t(x, y, z) = \frac{\partial s}{\partial x}\mathbf{x} + \frac{\partial s}{\partial y}\mathbf{y} + \frac{\partial s}{\partial z}\mathbf{z}\frac{\partial\phi_t}{\partial s}, \quad (18)$$

where

$$\phi_t(x, y, z) = -\frac{1}{2\pi}\int_T u_t(x', y', z')\frac{\exp^{-jks}}{s} dT$$

Here, u_t is the normal velocity of the transducer with a rigid baffle. Since the conical surface is divided into many plane reflectors, the incident wave at each acoustic windows can be assumed as a locally plane wave (i. e. $kr \gg 1$). Thus the ∇ operates on the mirror surface (x, y, z)

$$\mathbf{u}_i(x, y, z) = -j\mathbf{k}_i\phi_i, \quad (19)$$

where

$$\mathbf{k}_i = \frac{(x-x')}{s}\mathbf{x} + \frac{(y-y')}{s}\mathbf{y} + \frac{(z-z')}{s}\mathbf{z}$$

A design criterion was that rays from the transducer be totally reflected at the mirror surface due to an incident angle in excess of the critical angles for a water-steel surface. Using the reflection law at the boundary

$$(\mathbf{u}_i - \mathbf{u}_r)\times\mathbf{n} = 0,\ (\mathbf{u}_i + \mathbf{u}_r)\cdot\mathbf{n} = 0$$

the reflected wave velocity, ur, can be calculated to satisfy that the normal velocity at the mirror surface is zero.

$$\begin{bmatrix} u_{rx} \\ u_{ry} \\ u_{rz} \end{bmatrix} = \begin{bmatrix} 1-2n_x^2 & -2n_xn_y & -2n_xn_z \\ 2n_xn_y & 1-2n_y^2 & -2n_yn_z \\ -2n_xn_z & -2n_yn_z & 1-2n_z^2 \end{bmatrix}\cdot\begin{bmatrix} u_{ix} \\ u_{iy} \\ u_{iz} \end{bmatrix} \quad (21)$$

The boundary conditions used are those of a rigid, infinite planar baffle. Then, the Kirchhoff's diffraction integral using a free space Green's function and an in-phase mirror image source can be approximated by

$$\phi_s(\mathbf{r}) = -\frac{1}{4\pi}\int_M \frac{\exp^{-jkr}}{r}\mathbf{u}_r\cdot\mathbf{n}dM \quad (22)$$

In this case, the velocity right in front of the mirror, $\mathbf{u}_r$, is to be computed in advance to calculate the scattered field.

In the computation of approximate diffraction integrals, the transducer surface is divided using the condition that gives Fraunhofer approximation. The shortest distance between the mirror surface and transducer was used in evaluating the far-field conditions in [1]. Thus, the field potentials over the mirror surface can be calculated as the sum of the field contributions from each incremental source in the transducer. In similar manner, the mirror surface, reflecting either continuous or pulsed incident waves, is divided into a number of incremental areas making it possible to use the Fraunhofer approximation. Using acoustic reciprocity, the size of the mirror's incremental source is the same size of the transducer's incremental source. This condition guarantee that the phase error of the propagated wavefront from the transducer is negligible within the mirror's incremental areas.

2. Experimental Verification of Model

To verify the accuracy of the developed model, a 45° plane mirror geometry, as shown in Fig. 8 (a),

was employed. Since this configuration gives only a change in beam direction, its field characteristics are expected to correspond to a circular radiator case. The field pressure contour, normalized at each axial distance for a circular piston radius of 6λ, was calculated using the method presented in [1]. Figure 8 (b) shows that the developed model predicts the field patterns well for $F<10$. For the further approximate calculation of Eq. (22), only an illuminated mirror surface was included. The result still reveals good agreement.

To confirm the accuracy of the developed model with experiment, the field patterns at three axial distance were measured. Figure 9 shows the simulated and measured -3 dB lateral beam patterns agree well. The differences between the simulated and measured beam patterns are mainly due to the errors in positioning the probe in the z dimension and the spatial averaging effect of the finite aperture size of the hydrophone.

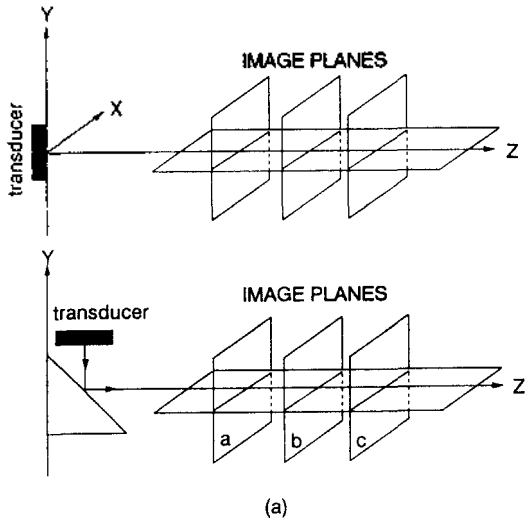

(a)

3. Field Characteristics of the Large-Scale FLUIC

Using the developed model, some important field parameters such as spatial resolution and the depth of field can be examined. There are two spatial resolution factors in a B-scan imaging. Resolution in the direction of acoustic wave propagation is called axial resolution. The resolution in this dimension is relatively unaffected by the presence or absence of focusing elements but is determined principally by the bandwidth of the transducer as discussed in section II. However, in the presence of a wide bandwidth signal, the frequency dependent absorption of the propagation medium affects the potential resolutions for deep fields [19]. Resolution in the scanning plane is called as the lateral resolution. Due to the asymmetry of the conical mirror, the lateral resolution should be defined both in the transverse and elevation dimension. The field can be determined using the method described in [1]. The time dependence of the transmitted pulse shape as well as its spatial variations can be investigated. The peak-detected *FWHM* (Full Width at Half Maximum) is, in general,

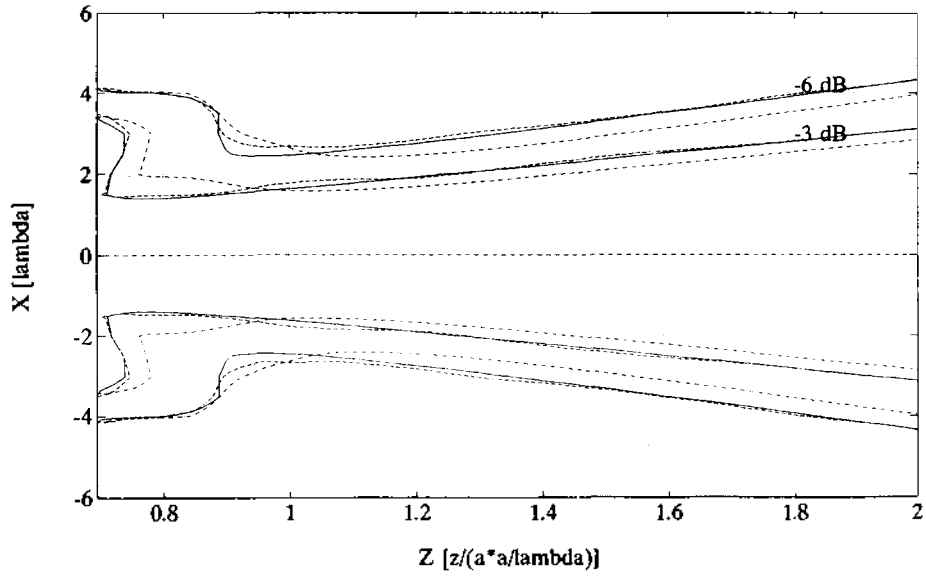

Fig. 8 The verification of the accuracy of the computational model. (a) Model Geometry. (b) Comparison of its off-axis accuracy (solid : the diffraction transfer approach, dash : the developed model using $F=10$, dashdot : the approximated calculation).

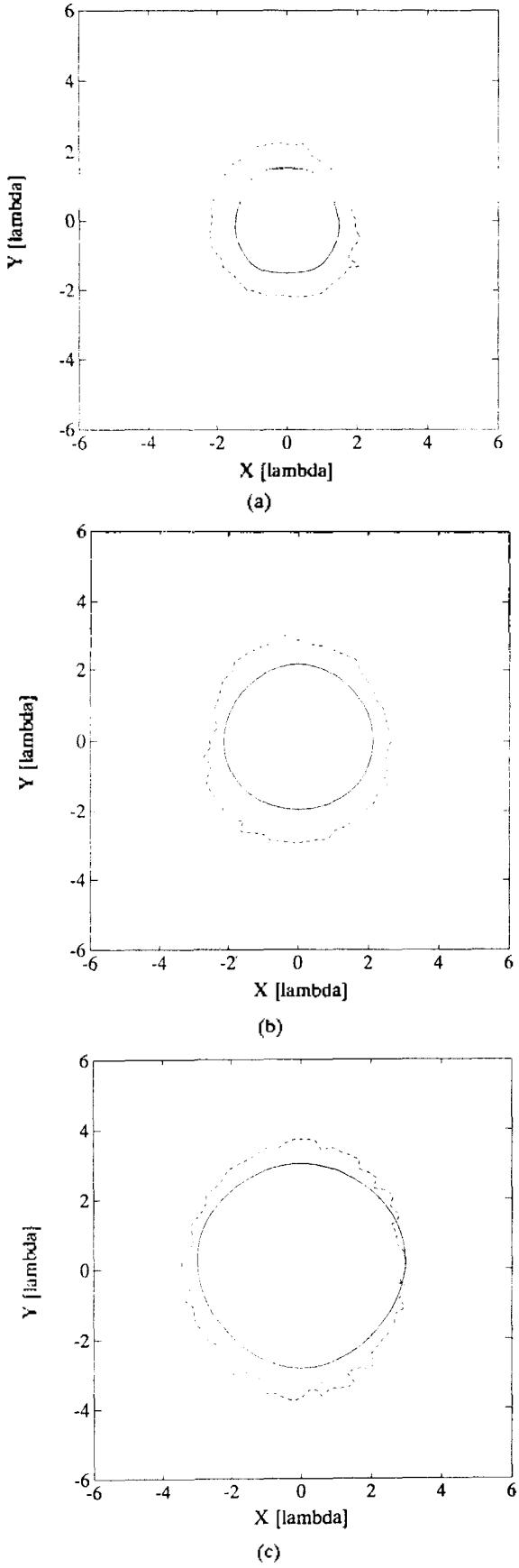

Fig. 9 The field patterns at three Z positions (solid : simulated, dashdot : measured). (a) $Z=0.78$. (b) $Z=1.34$. (c) $Z=1.9$.

very well approximated by the CW beamwidth evaluated at the pulse mean frequency. Thus, CW simulation provides a fairly good approximation of the field characteristics such as resolutions and depth of field.

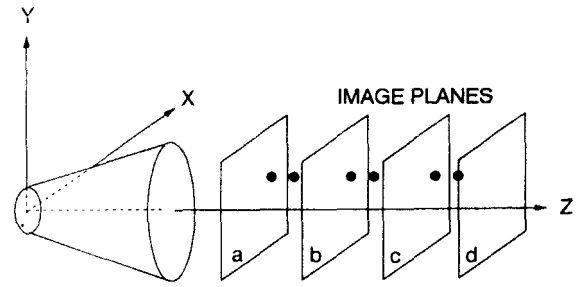

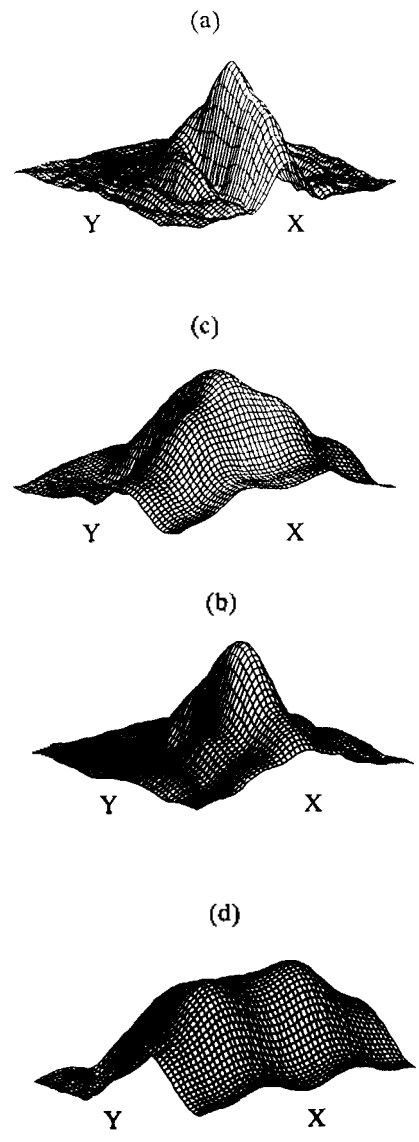

Fig. 10 Mesh plots of x-y field patterns of a FLUIC at $z=$ (a) 25λ : (b) 35λ : (c) 45λ : and (d) 55λ.

The field characteristics of the FLUIC was investigated. The transducer element was located at the center ($z_l = 10\lambda$) of the translational axis. The range of the scanned field was : $-6\lambda < x < 6\lambda$, $15\lambda < y < 30\lambda$, $25\lambda < z < 60\lambda$. This 3-D volume was scanned linearly in 0.25λ steps for the purpose of comparison with experimental results, which are presented in the next chapter. The computation model used in the simulation was the rigid secondary source case. Figure 10 illustrates the typical mesh surface plots of the 2-D beam patterns of a FLUIC at various image planes. The asymmetry of beam pattern in the transverse dimension results from the different curvatures of the conical mirror. As the axial distance increases, the beam patterns become broader. The beam patterns in the bottom side have broader beamwidth as expected from the results of the ray tracing method in section II. 3. In this geometry, for $z > 55\lambda$, the peak position occurs off-axis, as shown in Fig. 10 (d).

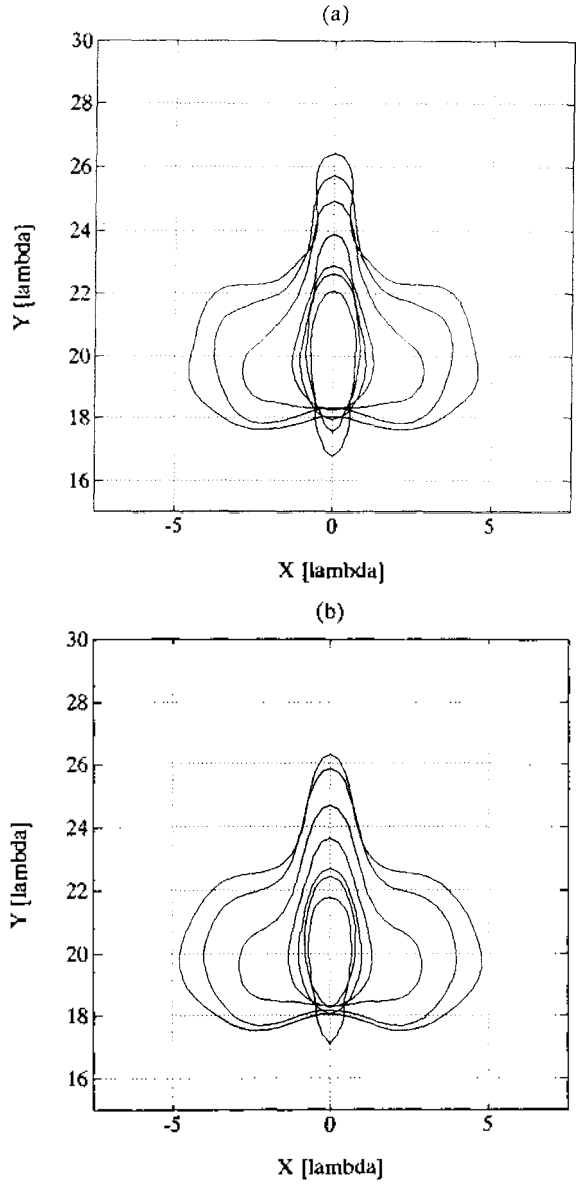

Fig. 11 Contour plots (-3 dB) at image planes from $z = 25\lambda$ to $z = 55\lambda$ in steps of 5λ using : (a) $F = 10$: (b) $F = 20$.

Figure 11 show the -3 dB lateral resolution from $z = 25\lambda$ to $z = 55\lambda$ in 5λ steps. The resolution in both transverse and elevation dimensions decrease as the axial distance increases. The transverse resolution is less than 2λ from $z = 25\lambda$ to $z = 40\lambda$. This implies that the transverse resolution will suffer if a large depth of field is desired. The elevation resolution is about 4λ to 6λ in this range. Compared to the transverse dimension, the image quality in this dimension would be relatively poor due to the low elevation resolution.

Up to this point, only the transmit field characteristics have been addressed. In pulse-echo imaging, the lateral resolution is ultimately limited by the pulse-echo response of the transducer as it detects the pressure waveform reflected by small targets. The sensitivity to off-axis isotropic reflectors, which is usually called the lateral point response, can be approximated by simple multiplication of the transmit and receive profile. The system transfer function, H_{PE}, for a point and rigid target is given by linear system analysis [20]

$$H_{PE}(\mathbf{r}, \omega) = H_T(\mathbf{r}, \omega) H_R(\mathbf{r}, \omega) \tag{23}$$

where H_T and H_R represent the one-way transmit and receive transfer function, respectively. When the same transducer is used to transmit and receive, the resolutions can, therefore, be approximated by the square of the one way distribution

$$FWHM_{PE} \cong FWHM_T. \tag{24}$$

VI. Conclusion

The conical mirror configuration for the transducer section of the FLUIC was designed, for IVUS imaging applications, using approximated ray tracing techniques. An extended version of the diffraction transfer function approach was employed to analyzed the field characteristics of the FLUIC. Good agree-

ment was obtained for the transducer configured with a simple planar reflector between measured and the simulated data.

As predicted from the results of the ray tracing method, the field characteristics of the designed FLUIC was shown to have the asymmetry of the beam pattern in the transverse dimension resulting from the different curvatures of the conical mirror. The transverse resolution is less than 2λ from $z=25\lambda$ to $z=40\lambda$. This implies that the transverse resolution will suffer if a large depth of field is desired. The elevation resolution is about 4λ to 6λ in this range. The resolution in both transverse and elevation dimensions decrease as the axial distance increases.

As a second part of this work, the fabrication and experimental results of a large-scale version of the transducer section of the FLUIC, operating at 2 MHz, will be mentioned. Also the accuracy of an extended version of the diffraction transfer function approach will be shown by predicting the field characteristics of the FLUIC.

REFERENCES

1. C. K. Lee and P. J. Benkeser, "A spatial fourier trans form approach to the calculation of the transient field of acoustic radiators," J. Acoust. Soc. Am., vol. 96, no. 1, pp. 545-551, 1994.
2. P. G. Yock, D. T. Linker, N. W. White, M. H. Rowe, and et al., "Clinical applications of intravascular ultrasound imaging in atherectomy," International Journal of Cardiac Imaging, no. 4, pp. 117-125, 1989.
3. N. G. Pandian, A. Weintraub, S. L. Schwartz, and et al., "Intravascular and intracardiac ultrasound imaging : current research and future directions," Echocardiography, vol. 7, no. 4, pp. 377-387, 1990.
4. J. M. Hodgson, S. P. Graham, H. Sheehan, and A. D. Savakus, "Percutaneous intracoronary ultrasound imaging : initial applications in patients," Echocardio graphy, vol. 7, no. 4, pp. 403-413, 1990.
5. K. H. Sheikh, K. Kisslo, and C. J. Davidson, "Interventional applications of intravascular ultrasound imaging : initial experience and future perspectives," Echocardiography, vol. 7, no. 4, pp. 433-441, 1990.
6. C. K. Lee and P. J. Benkeser, "Computationally efficient sound field calculations for a circular array transducer," IEEE Trans. Ultrason. Ferroelectr. Freq. Contr., vol. 39, no. 1, pp. 43-47, 1992.
7. M. S. Patterson and F. S. Foster, "Acoustic fields of conical radiators," IEEE Trans. Son. Ultrason., vol. SU-29, no. 2, pp. 83-92, 1982.
8. G. Salomonsson and B. Mandersson, "On ultrasound transducer with curved surface for improvement of lateral resolution," IEEE trans. Ultrasonics, Ferroelectrics, and Frequency Control, vol. 33, no. 6, pp. 740-746, 1986.
9. K. Yamada and H. Shimizu, "Variable aperture conical transducer," J. Acoust. Soc. Jpn., vol. 9, no. 5, pp. 211-215, 1988.
10. F. Sabet-Peyman, R. T. Weverka, I. C. Chang, and P. Katzka, "Beam scanning and focusing of bulk acoustic waves," IEEE Ultrasonic Symposium, pp. 424-429, 1984.
11. R. C. Addison and R. K. Elsley, "Side-looking microscope for interior inspection of holes," IEEE Ultrasonic Symposium, pp. 584-587, 1984.
12. C. K. Lee and P. J. Benkeser, "Investigation of a forward-looking IVUS imaging transducer," IEEE Ultrasonic Symposium, pp. 691-694, December,1991.
13. B. A. Auld, Acoustic Fields and Waves in Solids, vol. 2, A Wiley-Interscience Publication, 1973.
14. C. B. Burckhardt, H. Hoffmann, and P. A. Grandchamp, "Ultrasound axicon : a device for focusing over a large depth," J. Acoust. Soc. Am., vol. 54, no. 6, pp. 1628-1630, 1973.
15. Y. Sugawara, J. Kushibiki, and N. Chubachi, "Theoretical analysis on acoustic fields formed by focusing devices in acoustic microscopy," IEEE Ultrasonic Symposium, pp. 783-788, 1986.
16. S. Fujiwara, "Optical properties of conical surface, I. reflecting cone," J. Acout. Soc. Am., vol. 52, no. 3, pp. 287-292, 1962.
17. D. Roberti, R. Ludwig, and F. J. Looft, "A general-purpose computer program for studying ultrasonic beam patterns generated with acoustic lenses," IEEE Trans. on Instrumentattion and Measurement, vol. 37, no. 1, pp. 90-94, 1988.
18. M. Born and E. Wolf, Principles of Optics, Sixth Edition, Pergamon Press, 1980.
19. R. Lerch and W. Friedrich, "Ultrasound fileds in attenuating media," J. Acoust. Soc. Am., vol. 80, no. 4, pp. 1140-1147, 1986.
20. P. R. Stepanishen, "Pulsed transmit/receive response of ultrasonic piezoelectric transducers," J. Acoust. Soc. Am., vol. 69, no. 6, pp. 1815-1827, 1981.

▲이 찬 길 1958년 9월 1일생

1981년 2월 : 한양대학교 전자공학과(공학사)

1983년 2월 : 서울대학교 전자공학과(공학석사)

1992년 3월 : 미국 Georgia Inst. Tech. 전기공학과(공학박사)

1983년 3월 ~ 1985년 9월 : 한국전자통신연구소 TDX 개발단

1992년 3월 ~ 1994년 2월 : 한국전자통신연구소 이동통신연구단

1994년 3월 ~ 1995년 2월 : 경북대학교 전자공학과 전임강사

1995년 3월 ~ 현재 : 한양대학교 공학대학 전자공학과 조교수